

# Design of single-phase high-entropy alloys composed of low thermal neutron absorption cross-section elements for nuclear power plant application



C. Xiang<sup>a,b</sup>, E.-H. Han<sup>b,\*</sup>, Z.M. Zhang<sup>b</sup>, H.M. Fu<sup>c</sup>, J.Q. Wang<sup>b</sup>, H.F. Zhang<sup>c</sup>, G.D. Hu<sup>c,d</sup>

<sup>a</sup> School of Materials Science and Engineering, Northeastern University, Shenyang, 110819, China

<sup>b</sup> CAS Key Laboratory of Nuclear Materials and Safety Assessment, Institute of Metal Research, Chinese Academy of Sciences (CAS), Shenyang, 110016, China

<sup>c</sup> Shenyang National Laboratory for Materials Science, Institute of Metal Research, Chinese Academy of Sciences, Shenyang, 110016, China

<sup>d</sup> School of Materials Science and Engineering, University of Science and Technology of China, Shenyang, 110016, China

## ARTICLE INFO

### Keywords:

High-entropy alloys  
Alloy design  
Mechanical properties  
Nuclear power plant  
Accident tolerant fuel

## ABSTRACT

Two quinary high-entropy alloys MoNbCrVTi and MoNbCrZrTi were designed and prepared for the two following goals. The first goal is to search for single-phase high-entropy alloys composed of low thermal neutron absorption cross-section elements, and the second goal is to verify the validity of the empirical parameters calculation and CALPHAD (acronym of CALculation of PHase Diagrams) calculation in the initiatory selection process of desired alloys from numerous candidates. The density, hardness, microstructure, and compressive mechanical properties of the two alloys were preliminarily investigated, and the phase formation of these two alloys was also discussed. The MoNbCrVTi alloy consists of a single BCC phase with typical dendritic microstructure, while the MoNbCrZrTi alloy mainly consists of a BCC phase plus a C15 Laves phase. The densities of the as-cast MoNbCrVTi and MoNbCrZrTi alloys were determined to be  $7.30 \pm 0.01$  and  $7.33 \pm 0.01$  g/cm<sup>3</sup>, respectively. The MoNbCrVTi alloy exhibits a hardness of  $494.4 \pm 7.7$  Hv, a high yield strength of 1281 MPa and a fracture strain of 9.4% at room temperature. By comparison, the MoNbCrZrTi alloy exhibits a hardness of  $552.9 \pm 8.6$  Hv, a higher yield strength of 1454 MPa but a lower fracture strain of 2.7%. The proposed two goals are basically achieved based on the preliminary results.

## 1. Introduction

Nuclear power has already been proved to be a kind of reliable, environmentally sustainable, clean and cost-effective energy since its extensive utilization from the 1970s. Up to July 2018, there are total 453 nuclear power reactors in operation worldwide, and about 65% of them are pressurized water reactors (PWRs), followed by boiling water reactors (BWRs) and pressurized heavy water reactors (PHWRs) about 17% and 11%, respectively [1]. Zirconium alloys, such as Zr-2 and Zr-4, were widely used as fuel cladding materials for LWRs due to their low thermal neutron absorption cross-section, excellent corrosion resistance under normal operating conditions, adequate mechanical properties and good thermal conductivity [2]. Newly developed zirconium alloys (such as E635, Zirlo and M5) with significant improvement with regard to corrosion resistance and mechanical properties have been applied to nuclear reactors to achieve higher coolant temperature, higher fuel burnup, higher fuel duty and longer fuel cycle [2,3]. However, the recent Fukushima Daiichi accident happened in 2011 underlined the inherent demerits of zirconium alloys. In the case of a loss-of-coolant

accident (LOCA), zirconium alloys experienced severe strength loss and rapid high-temperature steam oxidation at  $T > 1200$  °C [4]. Later, the concept of accident tolerant fuel (ATF) was proposed to achieve higher safety margins under accident scenarios. So far, three general strategies have been proposed to develop new ATF claddings: modification of current Zr-based alloys via metallurgical composition and/or processing (including coatings on existing Zr-based alloys) to further improve oxidation resistance, replacement of present Zr-based alloys with an alternative high-performance cladding materials and replacement of the current monolithic ceramic oxide fuel with alternative fuel forms [3,5]. Extensive studies have been conducted to explore the feasibility of advanced ATF claddings and significant progress has been achieved [4,6–12].

Recently, a new class of materials termed high-entropy alloys (HEAs) [13] have attracted an ever-increasing amount of interest from academia and industries for their unique microstructures and outstanding mechanical properties. HEAs are generally defined as alloys composed of five or more principal constituents in equimolar or near-equimolar ratios and each prime element has an atomic concentration

\* Corresponding author.

E-mail address: [ehhan@imr.ac.cn](mailto:ehhan@imr.ac.cn) (E.-H. Han).

between 5 and 35% [13,14]. This innovative design strategy notably expands the field of multi-component alloys. In spite of five or more alloying elements in a typical equimolar HEA, most reported alloys are found to have only a simple solid-solution phase such as CoCrFeNiMn with a face-centered cubic (FCC) structure [15] and TaNbHfZrTi with a body-centered cubic (BCC) structure [16]. HEAs possess many merits such as high strength [17,18], irradiation resistance [19–21], good ductility [16,22], softening resistance [23,24], corrosion and oxidation resistance [25–27]. These advantages indicate that HEAs may have the potential for nuclear applications. Yet, most of the reported HEAs are composed of post-transition elements or refractory metals and the attention are mainly paid to the microstructure and mechanical properties as well as the phase formation rules. The work on the alloy design of HEAs for nuclear application and the evaluation of HEAs in simulated LWRs environment is highly limited. For example, the Cantor alloy CoCrFeNiMn with an FCC crystal structure and the AlCoCrFeNi alloy with a BCC crystal structure have been extensively investigated [15,28–33], another typical single-phase TaNbHfZrTi alloy with a BCC structure was also been well studied [16,34,35]. While for nuclear application, especially for ATF claddings, Co and Hf are unsuitable because of their high neutron absorption cross-sections. Therefore, it is worthwhile to design HEAs containing elements with low thermal neutron cross-section, high thermal conductivity, and excellent corrosion resistance at high temperatures in high-pressure water, air and steam, high melting point and stable phase structure up to elevated temperatures. By now, it seems to be a formidable task to meet all these requirements synchronously. However, several publications show the possibility to apply HEAs in the nuclear industry. The high-entropy alloys show excellent radiation resistance as indicated by recent studies [19,20,36,37]. In terms of corrosion resistance, Xiang et al. [27] studied the repassivation kinetics of three high-entropy alloys in high temperature pressurized water by rapid scratch technique [38], and the results were compared with a 690TT nickel-based alloy. It is found that the repassivation rates of the three high-entropy alloys and 690TT alloy are ranked as following: TaNbHfZrTi > Co<sub>1.5</sub>CrFeNi<sub>1.5</sub>Ti<sub>0.5</sub>Mo<sub>0.1</sub> > 690TT > AlCoCrFeNiSi<sub>0.1</sub>. Zhang et al. [39] recently developed a novel AlCrMoNbZr HEA coating deposited on N36 zirconium alloy using magnetron co-sputtering technique. The results show that the HEA coating contained a composite of amorphous and bcc-structured nanocrystals, and the coating shows high adherence to the substrate. Moreover, the corrosion tests were performed in pure water with 1000 ppm boron, 3.5 ppm lithium and < 10 ppm oxygen for 30 days at 360 °C and 18.7 MPa, and the weight gain of the coated samples was 8.8 mg/dm<sup>2</sup>, which was almost 3 times lower than that of the N36 substrate. Hence, they concluded that the AlCrMoNbZr HEA coating can be used as a promising ATF candidate material to improve the corrosion resistance of Zr-based alloys. Even though other performances of the coating such as the penalty to neutron economy and thermal conductivity have not been thoroughly studied, but the results can still shed some lights on the development of HEAs for nuclear applications.

In the present work, eight elements with low thermal neutron cross-sections are first chosen as alloying elements to design HEAs after careful scrutiny of the periodic table of the elements. The characteristic properties of the elements are given in Table 1. Current work is focused on quinary HEAs in order to simplify the selection process. So there are total  $C_8^5 = 56$  potential alloys to be investigated, and that would be a daunting task using trial and error method. On the contrary, in the first step, the combination of empirical parameters calculation and CALPHAD calculation are carried out to quickly pick out the desired alloys. The detailed information will be given in Section 2.1. And finally, two quinary HEAs MoNbCrVTi and MoNbCrZrTi were designed and prepared in this work. The density, hardness, microstructure, and compressive mechanical properties were preliminarily investigated. The motivation of current work is twofold. Firstly, it is worthwhile to search for single-phase HEAs composed of elements with low thermal neutron absorption cross-sections, and then further modifications can be

**Table 1**

Atomic weight ( $A_r$ ), density ( $\rho$ ), atomic radius ( $r$ ), melting point ( $T_m$ ), lattice constant ( $a$ ), Vickers hardness ( $Hv$ ), Young's modulus ( $E$ ), thermal neutron absorption cross-section ( $\sigma_A$ ), thermal conductivity ( $\lambda$ ), valence electron concentration (VEC) of the pure Zr, Nb, Fe, Mo, Cr, Ni, V and Ti elements [44–48].

Element	Zr	Nb	Fe	Mo	Cr	Ni	V	Ti
$A_r$	91.22	92.91	55.85	95.95	52	58.69	50.94	47.87
$\rho$ , g/cm <sup>3</sup>	6.51	8.57	7.87	10.28	7.14	8.91	6.11	4.51
$r$ , Å	1.6	1.43	1.24	1.36	1.25	1.25	1.32	1.46
$T_m$ , °C	1855	2477	1538	2623	1907	1455	1910	1668
$a$ , Å	3.582	3.301	286.6	3.147	2.884	3.530	3.024	3.276
$Hv$ , kgf/mm <sup>2</sup>	92	135	62	156	108	65	64	99
$E$ (GPa)	68	105	211	329	279	200	128	116
$\sigma_A$ (barn)	0.185	1.15	2.56	2.48	3.05	4.49	5.08	6.09
$\lambda$ , (W/(m·K))	22.7	53.7	80.2	138	93.7	90.7	30.7	21.9
VEC	4	5	8	6	6	10	5	4

achieved based on the single-phase alloy. Secondly, the authors want to verify the validity of the empirical parameters calculation and CALPHAD calculation in the initiatory selection of desired materials from numerous candidates. It will save a lot of time if the second goal would be achieved, thus the same methodology could be applied to design quaternary or senary HEAs based on the selected elements.

## 2. Experimental

### 2.1. Materials design

Eight elements (i.e. Zr, Nb, Mo, Cr, Fe, Ni, V and Ti) are first chosen as alloying elements to design equimolar HEAs. It can be seen from Table 1 that Ti has the largest value of thermal neutron cross-section 6.09 barns, while Zr has the smallest value of 0.185 b. Here, Al (0.231 b) has not been chosen for two following considerations. On one hand, Al has the lowest melting point (660 °C) compared to the other eight elements, and on the other hand, the mixing enthalpies between Al and other elements are relatively negative, which may lead to the appearance of secondary phase [40]. However, a small amount of Al may still need to be added to improve the corrosion and oxidation resistance, which is beyond the scope of the present work. The first goal of the present work is to search for single-phase HEAs with low thermal neutron cross-section elements. In this regard, it is necessary to apply the phase formation rules of HEAs which were proposed by the HEAs community. Empirical parameters including the enthalpy of mixing ( $\Delta H_{mix}$ ), the entropy of mixing ( $\Delta S_{mix}$ ), atomic size difference ( $\delta$ ),  $\Omega$ -parameter and the valence electron concentration (VEC) were calculated for the 56 potential candidates. The definition and elaboration of these parameters will be presented in Section 3.3 pertinent to specific alloys and their microstructures. Additionally, densities ( $\rho$ ) of the 56 alloys were also calculated. The calculated results of these parameters are given in Supplementary Table S1. Yang and Zhang et al. [41,42] suggested that simple solid solution phases tend to form at larger  $\Omega$  values ( $\Omega \geq 1.1$ ) and smaller  $\delta$  values ( $\delta \leq 6.6$ ). The criteria of the present work for alloys selection are mainly based on the  $\Omega$  and  $\delta$  values. The  $\Omega$ - $\delta$  plot of the 56 alloys is shown in Fig. 1. It can be seen from Fig. 1 that the ZrNbMoVTi alloy has the largest  $\Omega$  value ( $\Omega = 11.71$ ) and the  $\delta = 6.74$ , however, this alloy has already been studied by Wu et al. [43] and Senkov et al. [24]. The results showed that ZrNbMoVTi alloy is composed of two BCC phases and one Laves phase after homogeneous annealing treatment. Therefore, the ZrNbMoVTi alloy was not chosen currently for its microstructural complexity. Finally, the MoNbCrVTi ( $\Omega = 7.40$  and  $\delta = 5.54$ ) were chosen for searching for single-phase HEA due to its large  $\Omega$  value and small  $\delta$  value. Moreover, the MoNbCrZrTi with moderate  $\Omega$  value ( $\Omega = 5.53$ ) and relatively large  $\delta$  value ( $\delta = 8.13$ ) was intentionally chosen to demonstrate the validity of the empirical parameters calculation and CALPHAD calculation in materials selection. The CALPHAD calculations of the MoNbCrVTi and

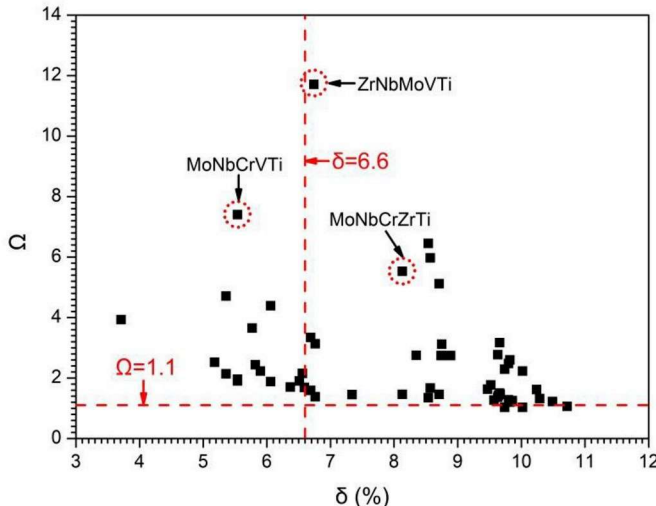


**Fig. 1.** The  $\Omega$ - $\delta$  plot of the 56 quinary HEAs composed of low thermal neutron cross-section elements.

MoNbCrZrTi alloys were performed using the ThermoCalc™ software with the TTNI8 thermodynamic database.

## 2.2. Materials preparation and characterization

The alloy ingots with nominal compositions of MoNbCrVTi and MoNbCrZrTi were prepared by vacuum arc melting in a water-cooled copper crucible under a Ti-gettered argon atmosphere. Rods, bars or lumps of the pure metals with purity higher than 99.5 wt% were

weighted to obtain the equimolar composition. In order to achieve a homogeneous distribution of the elements in the alloys, each alloy ingot was flipped over and then re-melted 5 times. The prepared button-shape ingots were about 44 mm in diameter and 10 mm in thickness, and had a lustrous surface, indicating that there was no oxidation during the vacuum arc melting.

The crystal structure was identified with an X-ray diffractometer (XPERT PRO) using Cu K $\alpha$  radiation, operated at a voltage of 40 kV and a current of 40 mA. The scanning range is from 20 to 100° with a scanning speed of 4°/min. The microstructure was analyzed using an SEM equipped with an energy dispersive spectrometer (EDS). Densities of the two alloys were measured by the hydrostatic weighing method. Vickers hardness was measured on polished cross-sectional surfaces using a 136° Vickers diamond pyramid with a load of 500 g applied for 15 s. The reported hardness values were the average of seven random measurements. Room temperature compression tests were performed on cylindrical specimens with diameters of 3 mm and heights of 6 mm using an Instron 5582 machine with an initial strain rate of  $10^{-3}$ /s.

## 3. Results and discussion

### 3.1. Thermodynamic modeling

CALPHAD modeling is demonstrated to be an effective method to predict the phase formation in HEAs such as CrNbTiVZr system [49], CrMo<sub>0.5</sub>NbTa<sub>0.5</sub>TiZr [50], MoNbTaTiV [51] and CrMoNbReTaVW [52], etc. The reported as-cast single-phase (BCC or FCC) HEAs such as MoNbTaTiV [51], NbTaTi(V,W) [53], MoNbTaVW [54], HfNbTaTiVZr [55], and CoCuFeMnNi [56] alloys were successfully predicted by CALPHAD modeling. Moreover, these single-phase HEAs usually show a typical dendritic microstructure and the microsegregation is

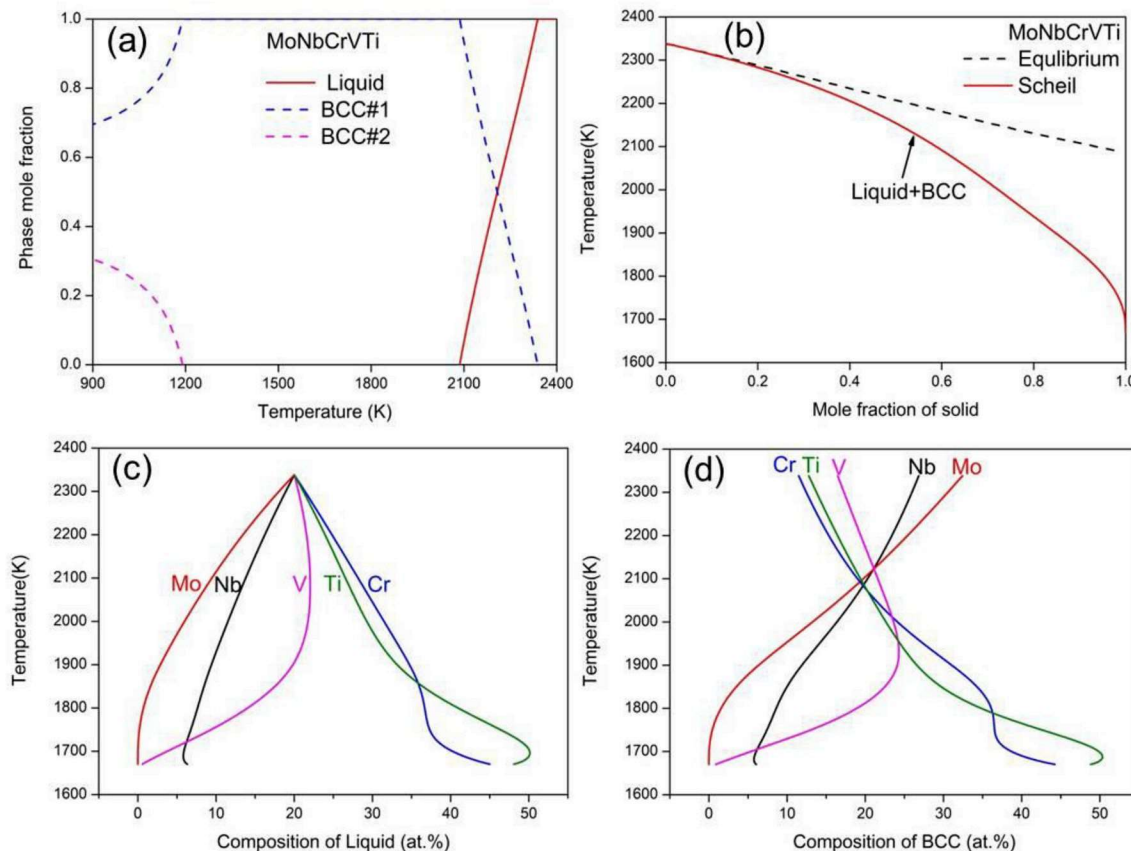


**Fig. 2.** (a) The calculated equilibrium phase diagram for MoNbCrVTi alloy. (b) Non-equilibrium solidification curve for MoNbCrVTi alloy using Scheil-Gulliver models. (c) Liquid phase composition (Scheil simulation). (d) BCC phase composition (Scheil simulation).

qualitatively agreed with the non-equilibrium (NE) solidification simulation. It is worth to note that the famous Cantor alloy FeCrMnNiCo are found to be a single-phase HEA with FCC crystal structure [15] and the alloy displays remarkable fracture toughness properties especially at cryogenic temperatures [57]. The phase formation were accurately predicted by CALPHAD modeling, as shown in Ref. [56]. The simulation results also indicate that the FCC phase is stable over a wide temperature range. Experimental results [58] show that the single phase state still remained even after annealing at 1000 °C for three days. The well agreement between the CALPHAD modeling and the experimental results indicates that the CALPHAD modeling is a robust and reliable tool to investigate the phase formation and stability of the HEAs. In the present work, the CALPHAD calculations were conducted for MoNbCrVTi and MoNbCrZrTi alloys by means of the ThermoCalc™ software with the TTNI8 thermodynamic database. The calculated equilibrium phase diagrams and NE solidification curves of MoNbCrVTi

and MoNbCrZrTi alloys are presented in Fig. 2 and Fig. 3, respectively. The equilibrium phase diagrams predict the formed phases under very low cooling rate which can't be reached in actual solidification process, while the NE solidification simulates the process with very large cooling rate which is close to the experimental condition, in other words, it can give information about the phase formation for an alloy in the as-cast state. The NE solidification was performed using Scheil-Gulliver models [59,60] which assume there is no diffusion in the solid phases, while the diffusion in the liquid phase is extremely fast. Hence, the conditions at the interface between the liquid and solid phases can be regarded as a local equilibrium with this approximation.

The calculated equilibrium phase diagram for MoNbCrZrTi alloy is presented in Fig. 2a. A primary BCC#1 phase starts to form at the liquidus temperature  $T_{liq} = 2338$  K and is completed at the solidus temperature  $T_{sol} = 2086$  K. The BCC#1 phase exists in a wide range from 2086K to 1190 K. As the temperature further decreases, it can be

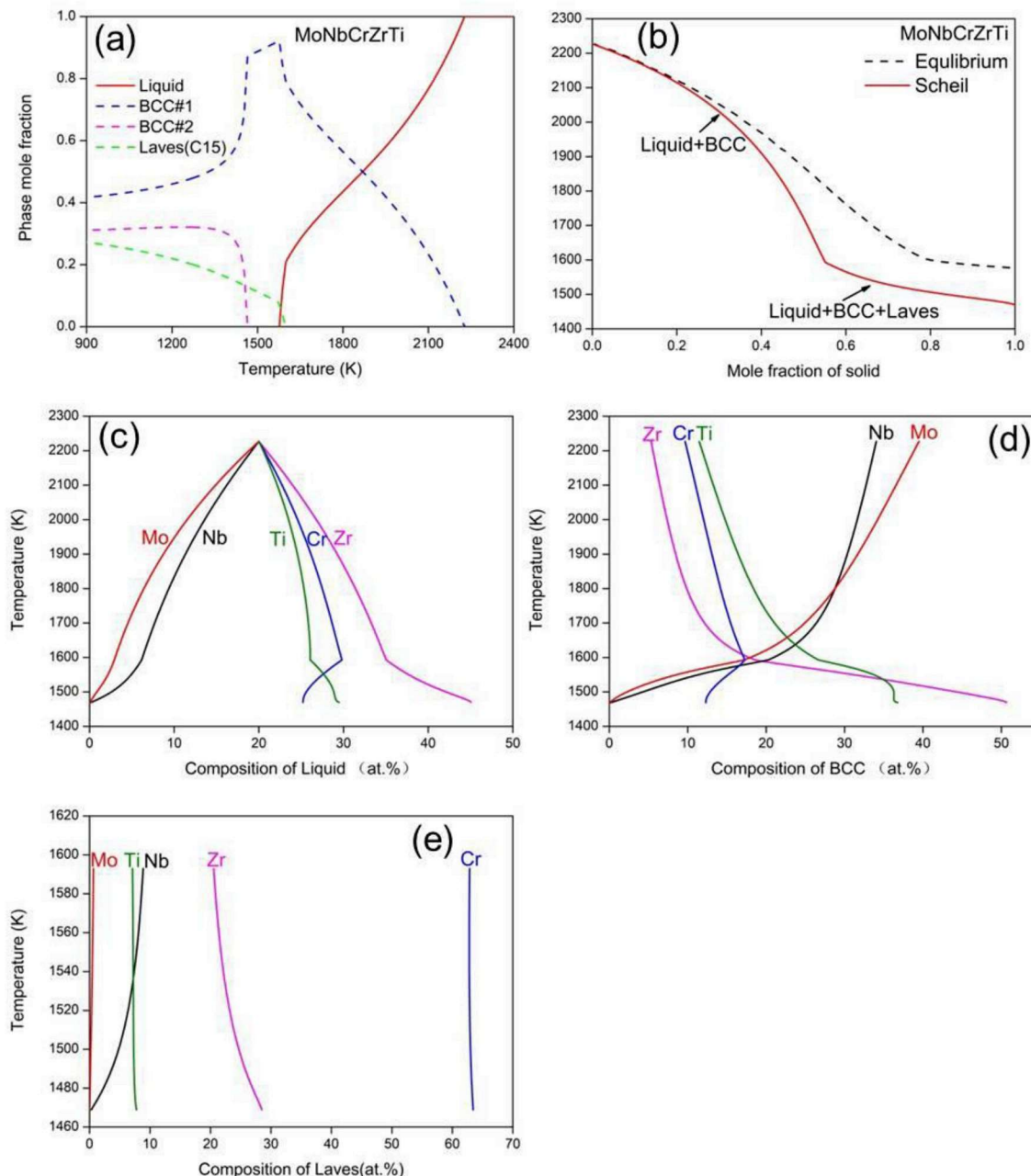


**Fig. 3.** (a) The calculated equilibrium phase diagram for MoNbCrZrTi alloy. (b) Non-equilibrium solidification curve for MoNbCrZrTi alloy using Scheil-Gulliver models. (c) Liquid phase composition (Scheil simulation). (d) BCC phase composition (Scheil simulation). (e) Laves phase composition (Scheil simulation).

**Table 2**

The chemical composition (in at.%), density ( $\rho$ ), and Vickers hardness ( $Hv$ ) of MoNbCrVTi and MoNbCrZrTi alloys.

Alloy	Mo	Nb	Cr	Zr	V	Ti	$\rho$ (g/cm <sup>3</sup> )	$\rho_{mix}$ (g/cm <sup>3</sup> )	$Hv$ (kgf/mm <sup>2</sup> )	$Hv_{mix}$ (kgf/mm <sup>2</sup> )
MoNbCrVTi	20.8	20.0	18.7	/	20.3	20.2	7.30	7.33	494.4 ± 7.7	112.6
MoNbCrZrTi	19.4	19.5	20.7	21.7	/	18.7	7.33	7.29	552.9 ± 8.6	117.4

seen that the BCC#1 phase starts to decompose at  $T_{dec} = 1190$  K. The ratio of the temperature range where the BCC#1 phase is stable over the solidus temperature (i.e.,  $(T_{sol} - T_{dec})/T_{sol}$ ) is determined to be 0.43. Gao [61] suggested that a ratio  $\geq 0.3$  typically favors the formation of a single-phase solid solution in the as-cast state. Indeed, the as-cast MoNbCrVTi alloy has been verified to be a single BCC phase with typical dendritic microstructure as shown later in section 3.3. Furthermore, the NE simulation (Fig. 2b) predicts only one BCC phase will be formed during the whole solidification which starts at  $T_{liq}^{NE} = 2338$  K and ends at  $T_{sol}^{NE} = 1669$  K, therefore the temperature range for NE solidification (669 K) is much broader than the equilibrium solidification (252 K). During the solidification process, the elemental compositions in both liquid and BCC phases vary significantly as the temperature decreases. The liquid is firstly depleted of elements with the high melting point such as Mo and Nb, whereas Cr and Ti are continuously enriched in the liquid (Fig. 2c). In the solid BCC phase, Mo and Nb are enriched since the solidification begins at 2338 K. At the end of solidification, the BCC phase is depleted by Mo and Nb, while Ti and Cr compositions are increased notably up to 45 – 48 at. % (Fig. 2d). The simulation results of the composition variation in MoNbCrVTi alloy imply that elemental segregation may occur in the as-cast alloy.

Fig. 3a shows the calculated equilibrium phase diagram of MoNbCrZrTi alloy. It shows that the primary BCC#1 phase starts to form at 2227 K, and is enriched with Mo and Nb, but heavily depleted of Zr and Cr. The Laves phase, which is enriched with Cr and Zr, forms at the later stage of solidification and the solidification is finally completed at 1576 K, then the Laves phase continues to form from the primary BCC#1 phase as the temperature decreases. A new BCC#2 phase also starts to form from the primary BCC#1 phase at  $T \leq 1465$  K. The BCC#2 phase is heavily enriched with Zr and Ti. The volume fraction of BCC#1, Laves and BCC#2 phase is 42.0%, 27.0% and 31.0%, respectively. On the other hand, the NE simulation predicts one BCC phase will form firstly at 2227 K and then another C15 Laves phase will appear at 1592 K. It is noted that the formation of this additional C15 Laves phase changes the slope of solidification curve notably, and the solidification process is completed at 1469 K. Thereby, according to the NE simulation, the MoNbCrZrTi alloy is predicted to consist of one BCC phase and one Laves phase with volume fraction of 85.2% and 14.8%, respectively. The compositions of the liquid, BCC and Laves phases during the NE solidification are presented in Fig. 3c, d and e. At the beginning of solidification, the liquid (Fig. 3c) is depleted of Mo followed by Nb, the contents of Cr, Ti and Zr are continuously increased until 1592 K when the Laves phase starts to form from the liquid, then Cr decreases abruptly, but Ti and Zr are still increased. The BCC phase (Fig. 3d) is enriched with Mo and Nb at the early stage of solidification, but depleted of Zr, Cr and Ti. As the temperature decreases, Mo and Nb are reduced continuously, whereas the content of Ti and Zr are increased up to 36.8 at.% and 50.6 at.%, respectively. The Laves phase is predicted to be mainly enriched with Cr and Zr with a stoichiometry close to Cr<sub>2</sub>Zr (Fig. 3e). Therefore, the NE simulation predicts that one BCC phase and one Laves phase will form in the MoNbCrZrTi alloy, while two BCC phases and one Laves phase will form according to the simulated equilibrium phase diagram. The real solidified microstructure will be somewhat between the phases predicted by the NE and equilibrium simulation under the two extreme conditions.

### 3.2. Density and hardness of MoNbCrVTi and MoNbCrZrTi alloys

The densities of the as-cast MoNbCrVTi and MoNbCrZrTi alloys were determined to be  $7.30 \pm 0.01$  and  $7.33 \pm 0.01$  g/cm<sup>3</sup>, respectively. Using the densities of the pure metals (Table 1) and the chemical composition of the alloys (Table 2), the density,  $\rho_{mix}$ , of an alloy composed of disordered solid solutions could be estimated by the rule of mixtures (ROM) [62]:

$$\rho_{mix} = \frac{\sum_{i=1}^n c_i A_i}{\sum_{i=1}^n \frac{c_i A_i}{\rho_i}} \quad (1)$$

Here  $c_i$ ,  $A_i$  and  $\rho_i$  are the atomic fraction, atomic weight and density of element  $i$ , respectively. The calculated densities,  $\rho_{mix}$ , for MoNbCrVTi and MoNbCrZrTi alloys are 7.33 and 7.29 g/cm<sup>3</sup>, which are very close to the measured results.

The ROM method is also applied to calculate the theoretical hardness of an alloy by the following equation:

$$Hv_{mix} = \sum_{i=1}^n c_i (Hv)_i \quad (2)$$

where  $(Hv)_i$  is the hardness of the  $i$ th element. The calculated theoretical hardness and the measured Vickers hardness of MoNbCrVTi and MoNbCrZrTi alloys are tabulated in Table 2. It could be seen that the Vickers hardness of MoNbCrVTi and MoNbCrZrTi alloys were determined to be  $494.4 \pm 7.7$  and  $552.9 \pm 8.6$  Hv, which are much higher than the theoretical values, 112.6 and 117.4 Hv, respectively. This huge discrepancy may result from solid-solution strengthening in these two alloys.

### 3.3. Crystal structure and microstructure

Fig. 4 shows the XRD patterns of the MoNbCrVTi and MoNbCrZrTi alloys. For the MoNbCrVTi alloy (Fig. 4a), all the XRD peaks are identified as a single BCC phase with the lattice constant  $a = 3.140$  Å. Again, using the chemical composition of the alloy (Table 2) and lattice constant of the pure metals (Table 1), the lattice constant of the disordered BCC solid solutions could be estimated using the ROM:

$$a_{mix} = \sum_{i=1}^n c_i a_i \quad (3)$$

Here  $a_i$  is the lattice constant of element  $i$ . The calculated lattice parameter of MoNbCrVTi alloy is 3.130 Å, which is slightly lower than the experimental value of 3.140 Å. The similar values of the experimental and calculated lattice constants indicate that MoNbCrVTi alloy is composed of a disordered solid-solution phase. Moreover, the absence of superlattice peaks also confirms this observation. For the MoNbCrZrTi alloy (Fig. 4b), two different phases can be identified from the XRD peaks. One is a disordered BCC phase (A2) and the other is an ordered Laves (C15) phase. The measured lattice constants for the BCC and C15 Laves phases are  $a = 3.215$  Å and  $a = 7.412$  Å, respectively. The calculated lattice constant of the BCC phase for the MoNbCrZrTi alloy is 3.235 Å, which is slightly larger than the experimental value of 3.215 Å.

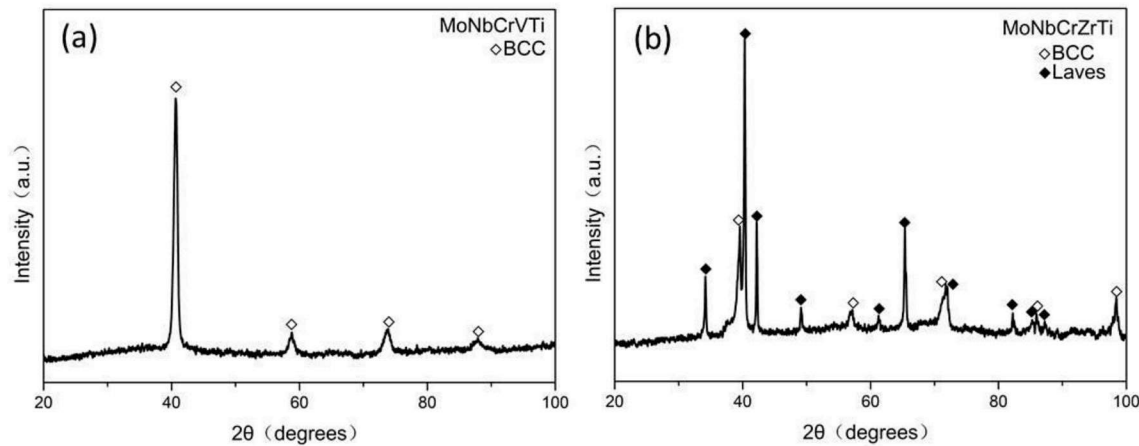


**Fig. 4.** X-ray diffraction patterns for the as-cast (a) MoNbCrVTi and (b) MoNbCrZrTi alloys.

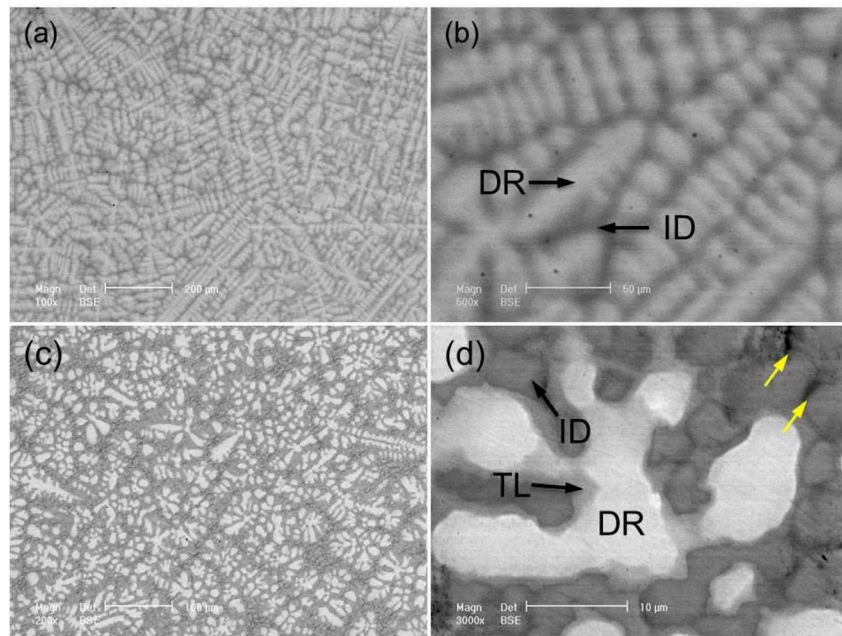


**Fig. 5.** SEM backscatter electron images of the as-cast MoNbCrVTi (a) and MoNbCrZrTi(c) alloys. (b) and (d) are higher magnification images of these two alloys.

**Fig. 5** presents the SEM backscattered electron (BSE) images of the MoNbCrVTi (**Fig. 5a** and b) and MoNbCrZrTi (**Fig. 5c** and d) alloys. It is clearly seen that the MoNbCrVTi alloy has a typical dendritic microstructure, indicating the elemental microsegregation occurs during the NE solidification (**Fig. 5a** and b). In agreement with the XRD results, the observed SEM results indicate no formation of other phases in the MoNbCrVTi alloy. The bulk composition of the alloy, the average composition of the dendrite arms and the averaged composition of the interdendritic regions are listed in **Table 3**. It is clearly seen that high melting point elements Mo and Nb preferentially segregate to the dendrite arms. The interdendrite (ID) is enriched with Cr and Ti, but Mo

and Nb is deficient. The V content in the ID is slightly higher than that in the dendrite (DR). Based on the average chemical composition of DR and ID (**Table 3**), the elemental segregation degree can be assessed by  $S_R$ , which is defined as following [63]:

$$S_R = C_{DR}/C_{ID} - 1 \quad (4)$$

Here  $C_{DR}$  and  $C_{ID}$  are the concentration of each element in the dendritic and interdendritic regions, respectively. The larger value of  $S_R$  means higher elemental segregation degree in the dendritic regions. On the contrary, the smaller value indicates higher elemental segregation level in the interdendritic regions. The calculated  $S_R$  values of Mo, Nb, Cr, V and Ti are +1.35, +0.27, -0.45, -0.10 and -0.29, respectively, which is largest for Mo but smallest for Cr. This implies that the DR is heavily enriched with Mo and ID is rich in Cr. The EDS mapping of the elements Mo, Nb, Cr, V and Ti in the MoNbCrVTi alloy shown in **Fig. 6** further consolidates this observation. Moreover, as described in section 3.1, it is shown that the NE solidification of the MoNbCrVTi alloy correctly predicts the chemical segregation occurrence in the as-cast state. Specifically, Mo and Nb tend to segregate into dendrite arms, while Cr and Ti segregate into the interdendritic regions. The semi-quantitative EDS analysis shown in **Table 3** is consistent with the

**Table 3**

The chemical composition (in at.%) of the as-cast MoNbCrVTi alloy using EDS analysis.

Region	Mo	Nb	Cr	V	Ti
Overall (4.25 mm <sup>2</sup> area)	20.8	20.0	18.7	20.3	20.2
Dendritic regions	27.7	22.2	14.1	18.3	17.7
Interdendritic regions	11.8	17.5	25.6	20.3	24.8

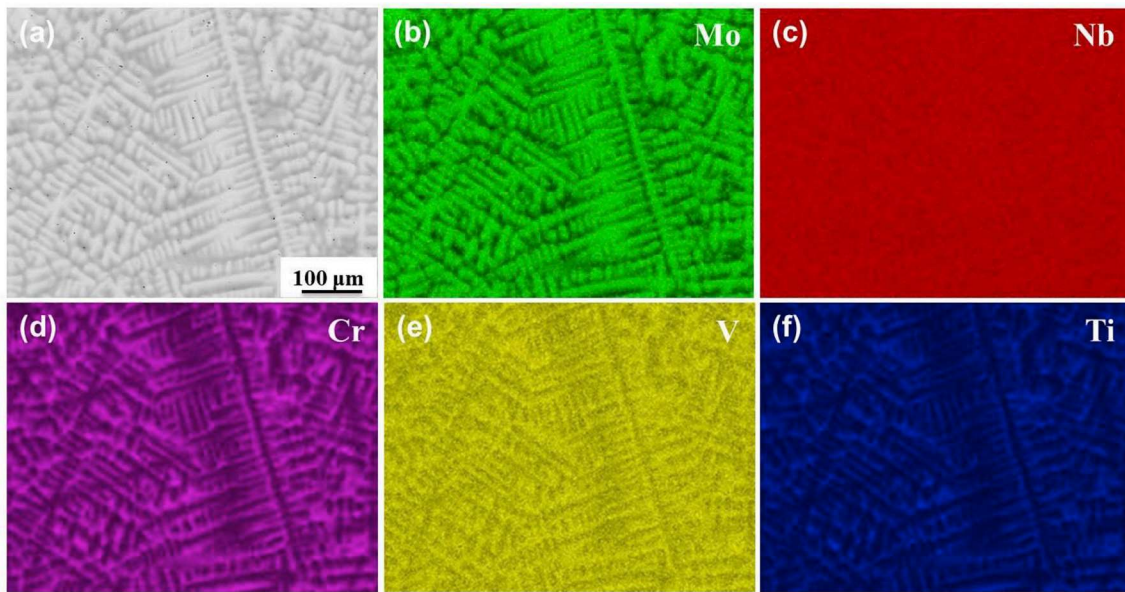


**Fig. 6.** The SEM backscattered electron image and EDS mapping of elements Mo, Nb, Cr, V and Ti in the as-cast MoNbCrVTi alloy.

simulation results. But the EDS mapping result indicates that Nb is almost homogeneously distributed in the alloy, which may be ascribed to the minor difference of Nb composition in the DR and ID.

The microstructure of MoNbCrZrTi alloy, as shown in Fig. 5c and d, seems to be much more complex than MoNbCrVTi alloy. Similarly, the as-solidified MoNbCrZrTi alloy also exhibits a dendritic microstructure (Fig. 5c). On the BSE images, the white regions are DR and the grey regions are ID (Fig. 5d). Higher magnification images reveal that a small number of dark regions are also presented in the interdendritic regions (shown in Fig. 5d by the yellow arrow). Additionally, a transition layer (TL) about 1 μm thickness can also be seen around the bright dendrites. Senkov et al. [47] previously had also found this kind of transition layer in a refractory NbCrMo<sub>0.5</sub>Ta<sub>0.5</sub>TiZr HEA. It can be clearly seen that the atomic number (Z) contrast between different phases in MoNbCrZrTi alloy is evident from backscatter electron (BSE) images due to chemical segregation in the as-cast microstructure. Thereby, the elemental distributions in the as-solidified MoNbCrZrTi

alloy were further examined using the EDS mapping, as shown in Fig. 7. The mapping results visually show that the DR is enriched with Mo and Nb, the ID is heavily enriched with Cr and Zr, and the TL is rich in Ti and Nb but depleted by Mo and Cr. The dark regions are heavily enriched with Zr and Ti, slightly rich in Nb, but depleted in Mo and Cr. The volume fractions of the bright dendrites together with the TL, interdendritic regions and dark regions are 37.0%, 60.6% and 2.4%, respectively.

The detailed chemical analysis results of these distinct regions using the EDS detector attached to the SEM are tabulated in Table 4. The element distributions in different regions are consistent with the EDS mapping results. Moreover, the XRD pattern of the as-cast MoNbCrZrTi alloy (Fig. 4b) confirms the presence of two phases, i.e., BCC and C15 Laves phases. As discussed in section 3.1, the simulated NE solidification of MoNbCrZrTi alloy predicts that one BCC phase and one Laves phase will form at the end of solidification, and the BCC phase is enriched with Mo and Nb, the Laves phase is enriched with Cr and Zr.

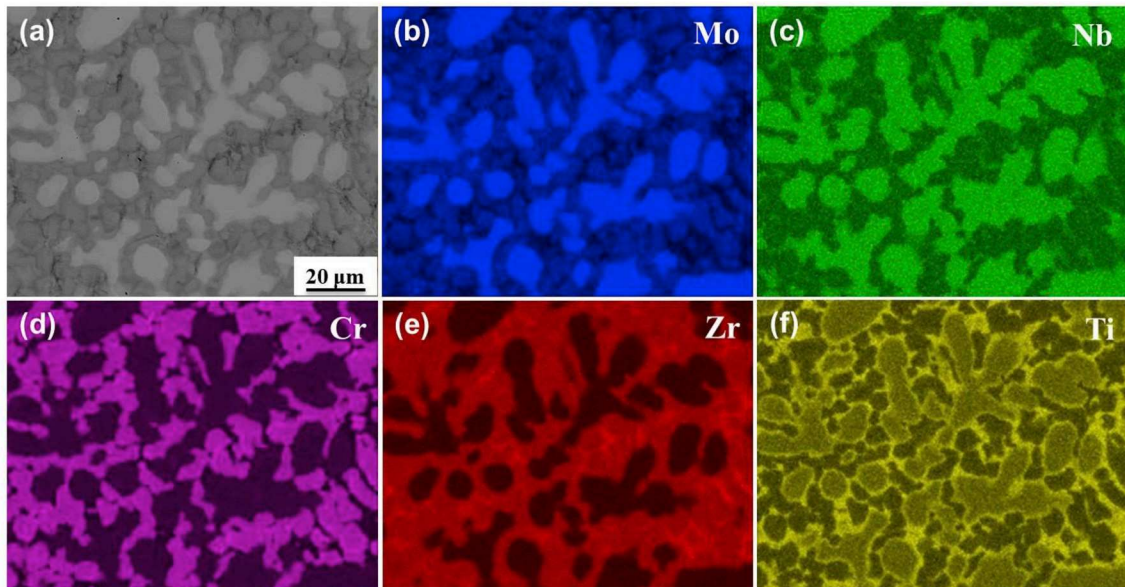


**Fig. 7.** The SEM backscattered electron image and EDS mapping of elements Mo, Nb, Cr, Zr and Ti in the as-cast MoNbCrZrTi alloy.

**Table 4**

The chemical composition (in at.%) of the as-cast MoNbCrZrTi alloy using EDS analysis.

Region	Mo	Nb	Cr	Zr	Ti
Overall (4.25 mm <sup>2</sup> area)	19.4	19.5	20.7	21.7	18.7
White regions	32.4	29.5	9.6	10.1	18.4
Transition layer	14.4	26.4	7.2	21.3	30.7
Grey regions	16.9	13.9	31.3	27.7	11.1
Dark regions	9.7	24.3	7.0	28.1	30.9

Thus, the bright dendrites are likely to be the BCC phase, while the interdendrites are enriched in Cr and Zr are likely to be the Laves phase. It is noted that the dark region is enriched with Ti and Zr but depleted in Mo and Cr. Based on the EDS mapping and semi-quantitatively chemical analysis results, the phase of the dark regions is denoted as Ti–Zr-rich phase here. In addition, the transition layer is rich in Ti–Nb but Mo–Cr depleted, the amount of Zr in the layer is close to the alloy composition. It can be seen that the composition of this layer is different from the composition of the other three phases. As previously stated, only BCC and Laves phases are identified from the XRD pattern for the as-cast MoNbCrZrTi alloy. Meanwhile, the amount of Ti-rich phase is not enough to be identified by the XRD analysis. Therefore, the layer may still retain the BCC structure based on an educated guess. However, the detailed microstructure of MoNbCrZrTi alloy needs to be further investigated in the future work.

Combining the CALPHAD calculations, XRD patterns and SEM/EDS analysis, it can be deduced that the (Mo, Nb)-rich BCC#1 phase first solidified from the liquid, as the temperature decreases, then the Laves phase starts to form from the liquid. When the solidification is completed, the BCC#1 phase decomposes to the Laves phase and a new BCC#2 phase. Hence it can be seen from the BSE images of MoNbCrVTi alloy that the BCC#1 phase is in the dendrite regions, whereas the Laves phase is in the interdendrite regions and a transition layer between these two phases seems to be the BCC#2 phase based on the educated guess. On the other hand, the slight discrepancy between the lattice parameters of BCC#1 and BCC#2 phase makes it very difficult to identify these two phases from XRD patterns. At last, a small amount of Ti–Zr-rich phase precipitated at relatively low temperature.

The elemental segregation is observed both in the as-cast MoNbCrVTi and MoNbCrZrTi alloys, which is mainly affected by the melting point differences (Table 1) and the mixing enthalpies (Fig. 8) among these alloying elements. During the solidification process, the elements with the high melting point such as Mo and Nb tend to segregate into the firstly solidified dendritic regions, while the low melting point elements tend to segregate into the later solidified interdendritic regions. This phenomenon is often observed in the HEAs, such as Al<sub>x</sub>HfNbTaTiZr [64], HfMo<sub>x</sub>NbTaTiZr [65] and CrMo<sub>0.5</sub>NbTa<sub>0.5</sub>TiZr [50] alloys, composed of alloying elements with larger melting point

differences. Besides, the mixing enthalpies among the alloying elements also exert a significant influence on the elemental distributions in an alloy, especially with a multiphase microstructure [66]. In general, if the mixing enthalpies for unlike atomic pairs with more negative values, ordering or intermetallic compounds prefer to form. On the contrary, the clustering or segregation will occur if the mixing enthalpies are much more positive as presented in Cu-containing HEAs AlCoCr-CuFeNi [30] and AlCrFeCuNi [67]. The disordered solid solutions prefer to form when the mixing enthalpies values are close to zero [68]. For the MoNbCrVTi alloy, since the mixing enthalpies of the unlike atomic pairs in this alloy do not show a large difference, the partitioning of elements in the dendrite and interdendrite is largely attributed to the melting point difference. While for the MoNbCrZrTi alloy, the mixing enthalpy of Cr–Zr has the most negative value of -12 kJ/mol, this might partly account for the enrichment of Cr and Zr in the Laves phase. It is noted that nano-size precipitates may be formed in the as-cast or annealed HEAs, as indicated in Refs. [69,70]. Only XRD and SEM measurements are insufficient to detect and characterize the precipitates. In future work, transmission electron microscope (TEM) and/or atom probe tomography (APT) analysis should be performed to further reveal the detailed microstructure.

There are four core effects underlying the unique microstructures and properties of high-entropy alloys including high-entropy effect, severe lattice distortion, sluggish diffusion and cocktail effects [14]. Among these, the high entropy effect is the most characteristic and important as implied by the name “high-entropy alloys”. The high mixing entropy could enhance the formation of solid solutions and make the microstructure simpler [14]. The entropy of mixing ( $\Delta S_{mix}$ ) is defined as follows:

$$\Delta S_{mix} = -R \sum_{i=1}^n c_i \ln c_i \quad (5)$$

in which  $R$ ,  $n$  and  $c_i$  are the gas constant, the total number of alloying elements, and the mole concentration of the  $i$ th element, respectively. However, only high mixing entropy could not ensure the formation of a single solid-solution phase which is crucial to the development of functional materials. Recently, CALPHAD modeling and empirical parameters are widely used to accelerate exploration of HEAs with solid-solution phases. The CALPHAD modeling for both alloys has been discussed in section 3.1, then the following discussion is about the relationship between phase formation and the empirical parameters which are based on thermodynamics and the geometry effect including  $\Delta S_{mix}$ , enthalpy of mixing ( $\Delta H_{mix}$ ), atomic size difference ( $\delta$ ) [71] and  $\Omega$ -parameter [41,42].

The  $\Delta H_{mix}$  is defined as:

$$\Delta H_{mix} = \sum_{i=1, i \neq j}^n 4\Delta H_{ij}^{mix} c_i c_j \quad (6)$$

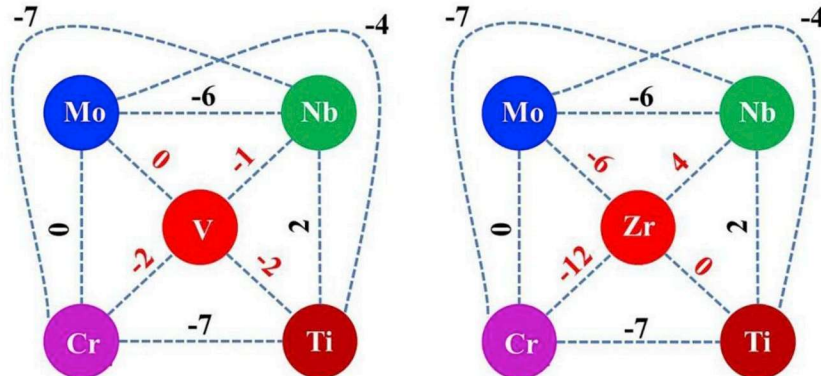


Fig. 8. Mixing enthalpy (kJ/mol) of unlike atomic pair used in MoNbCrVTi and MoNbCrZrTi alloys [40].

**Table 5**

The enthalpy of mixing ( $\Delta H_{mix}$ ), the entropy of mixing ( $\Delta S_{mix}$ ), melting point ( $T_m$ ),  $\Omega$  parameter, atomic size difference ( $\delta$ ) and valence electron concentration (VEC) values for MoNbCrVTi and MoNbCrZrTi alloys.

Alloy	$\Delta H_{mix}$ (kJ/mol)	$\Delta S_{mix}$ (J/mol K)	$T_m$ (K)	$\Omega$	$\delta$ (%)	VEC
MoNbCrVTi	−4.32	13.38	2390	7.40	5.54	5.20
MoNbCrZrTi	−5.76	13.38	2379	5.53	8.13	5.00

where  $\Delta H_i^{mix}$  is the enthalpy of mixing between the  $i$ th and the  $j$ th elements calculated by Miedema's model at a liquid state [40].

The  $\delta$  parameter is calculated by the following equation:

$$\delta = \sqrt{\sum_{i=1}^n c_i (1 - r_i/\bar{r})^2} \quad (7)$$

where  $r_i$  is the atomic radius of the  $i$ th element, and  $\bar{r}$  is the average atomic radius of all elements in an alloy (i.e.  $\bar{r} = \sum_{i=1}^n c_i r_i$ ).

The  $\Omega$  parameter is calculated using the following equation:

$$\Omega = T_m \Delta S_{mix} / |\Delta H_{mix}| \quad (8)$$

where  $T_m$  is the average melting point of the alloy ( $T_m = \sum_{i=1}^n c_i T_m^i$ , where  $T_m^i$  is the melting point of element  $i$ ).  $\Delta S_{mix}$  and  $\Delta H_{mix}$  are the aforementioned entropy of mixing and enthalpy of mixing, respectively.

In addition, Guo et al. [72] have proposed another criterion, the valence electron concentration (VEC), to predict the stable structure in solid-solution phases and have concluded that FCC phases are more stable with higher VEC ( $\geq 8$ ) and BCC phases are more stable with lower VEC ( $< 6.87$ ). The mixture of the BCC phase and FCC phase could coexist when  $8 > VEC \geq 6.87$ . The VEC is defined as:

$$VEC = \sum_{i=1}^n c_i (VEC)_i \quad (9)$$

where  $(VEC)_i$  is the VEC of element  $i$ .

The calculated empirical parameters for the MoNbCrVTi and MoNbCrZrTi alloys are listed in Table 5. Zhang et al. [71] first suggested if  $-15 \leq \Delta H_{mix} \leq 5$  kJ/mol,  $12 \leq \Delta S_{mix} \leq 17.5$  J/K·mol and  $\delta \leq 6.5\%$ , then solid solutions will form in HEAs. Later, two parameters,  $\Omega$  ( $\geq 1.1$ ) and  $\delta$  ( $\leq 6.6\%$ ), were proposed to predict the formation of solid-solutions in HEAs [41,42]. For both studied alloys, the values of  $\Delta H_{mix}$  and  $\Delta S_{mix}$  are within the aforementioned range. The values of  $\Omega$  for both alloys are much larger than 1.1, but the  $\delta$  values are different. The  $\delta$  value for MoNbCrVTi is 5.54% which is less than 6.6%; however, the  $\delta$  value for MoNbCrZrTi alloy is 8.13% which is much larger than 6.6%. Therefore, a single solid-solution phase may form in the MoNbCrVTi alloy while multi-phase may form in the MoNbCrZrTi alloy. On the other hand, the VEC values for these two alloys are 5.20 and 5.00, respectively, which are less than 6.87. This indicates that MoNbCrVTi and MoNbCrZrTi alloys are mainly composed of BCC phases. In a word, the experimental results are well agreed with the prediction of empirical parameters.

### 3.4. Mechanical properties

The compressive engineering stress-strain curves for MoNbCrVTi and MoNbCrZrTi alloys at room temperature are shown in Fig. 9. The 0.2% offset yield strength ( $\sigma_{0.2}$ ), compressive strength ( $\sigma_p$ ) and fracture strain ( $\epsilon_f$ ) are also tabulated in Table 6. The MoNbCrVTi and MoNbCrZrTi alloys show the plastic yielding at 1281 MPa and 1454 MPa, respectively. The MoNbCrVTi alloy achieved the compressive strength of 1677 MPa at  $\epsilon = 7.8\%$ , while the compressive strength of MoNbCrZrTi alloy is 1655 MPa which is close to MoNbCrVTi alloy but achieved at smaller engineering strain  $\epsilon = 2.5\%$ . The fracture strain is 9.4% and 2.7% for MoNbCrVTi and MoNbCrZrTi alloys, respectively. The different mechanical behavior of the two alloys may be ascribed to

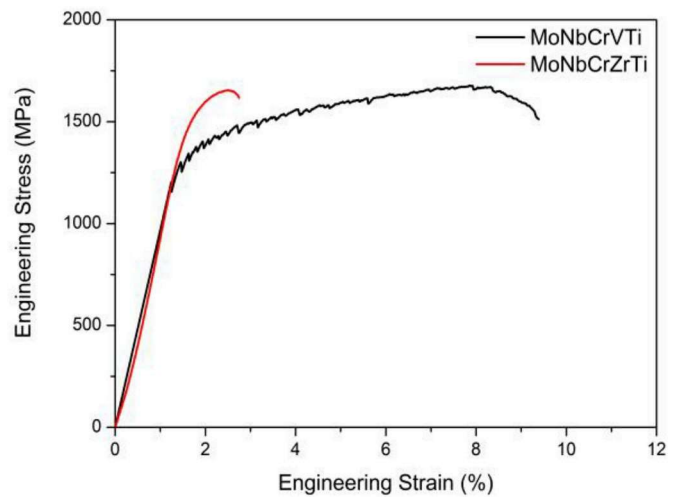


Fig. 9. Compressive engineering stress-strain curves of MoNbCrVTi and MoNbCrZrTi alloys.

**Table 6**

The 0.2% offset yield strength ( $\sigma_{0.2}$ ), compressive strength ( $\sigma_p$ ) and fracture strain ( $\epsilon_f$ ) of MoNbCrVTi and MoNbCrZrTi alloys.

Alloy	Yield stress, $\sigma_{0.2}$ (MPa)	Compressive stress, $\sigma_p$ (MPa)	Fracture strain, $\epsilon_f$ (%)
MoNbCrVTi	1281	1677	9.4
MoNbCrZrTi	1454	1655	2.7

two aspects. For the two quinary HEAs, MoNbCrVTi and MoNbCrZrTi, they all contain Mo, Nb, Cr and Ti, the former alloy has V with Vickers hardness 64 Hv while the latter alloy has Zr with a larger Vickers hardness 92 Hv. As mentioned earlier, the cocktail effect is one of the four core effects of HEAs [14]. The difference of Vickers hardness between V and Zr may contribute to the difference of the Vickers hardness and yield strength of the two alloys. On the other hand, the MoNbCrVTi alloy consists of a single BCC phase with typical dendritic microstructure, whereas the MoNbCrZrTi alloy is mainly composed of a BCC phase and a brittle Laves phase. It is believed that the different mechanical properties in the two alloys are mainly affected by the microstructural difference; in particular, the presence of brittle Laves phase in MoNbCrZrTi alloy could deteriorate its mechanical properties significantly.

The SEM images of fracture surfaces for MoNbCrVTi and MoNbCrZrTi alloys are shown in Fig. 10a and Fig. 10b, respectively. The cleavage planes, cleavage steps and river-like patterns can be clearly seen from the fracture surfaces of MoNbCrVTi alloy, which indicates that the fracture pattern is typical brittle cleavage fracture. The MoNbCrZrTi alloy exhibits quasi-cleavage fracture features as shown by the presence of river-like patterns and small size fracture facets on the fracture surface. As mentioned previously in section 3.3, the MoNbCrZrTi alloy is mainly composed of a BCC phase and a C15 Laves phase, the different fracture morphologies are believed to result from the microstructural difference between these two alloys.

### 4. Conclusions

The feasibility for designing single-phase HEAs composed of low thermal neutron cross-section elements were explored, and two quinary MoNbCrVTi and MoNbCrZrTi HEAs were designed and prepared. Density, hardness, microstructure and mechanical properties were investigated and the following conclusions can be drawn:

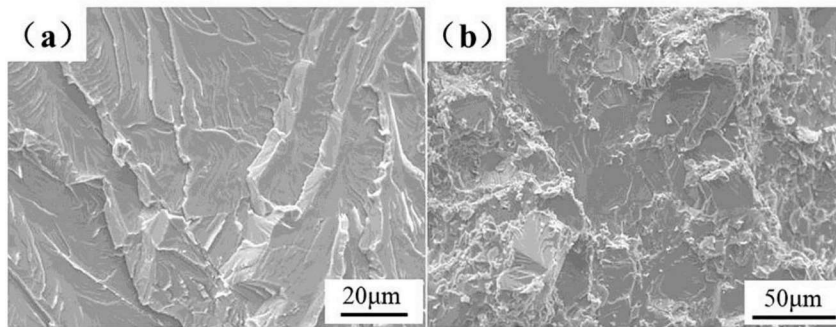


**Fig. 10.** Fracture surfaces of (a) MoNbCrVTi and (b) MoNbCrZrTi alloys after compression tests at room temperature.

- (1). A single-phase MoNbCrVTi alloy composed of low thermal neutron cross section elements are successfully designed via empirical parameters calculation and CALPHAD calculation.
- (2). The MoNbCrVTi alloy has simple BCC crystal structure and presents typical dendritic microstructure, the dendrite is enriched with Mo, while the interdendrite is enriched with Cr, V and Ti. The MoNbCrZrTi alloy mainly consists of a BCC phase plus a C15 Laves phase. In addition, another transition layer about 1  $\mu\text{m}$  thickness formed between the primary BCC phase and C15 Laves phase. And a small amount of Ti–Zr-rich phase also observed in the MoNbCrZrTi alloy.
- (3). The densities for the as-cast MoNbCrVTi and MoNbCrZrTi alloys were determined to be  $7.30 \pm 0.01 \text{ g/cm}^3$  and  $7.33 \pm 0.01 \text{ g/cm}^3$ , respectively. The MoNbCrVTi alloy exhibits a hardness of  $494.4 \pm 7.7 \text{ Hv}$ , a high yield strength of 1281 MPa, and fractured at a strain of 9.4% at room temperature. The MoNbCrZrTi alloy exhibits a hardness of  $552.9 \pm 8.6 \text{ Hv}$ , a higher yield strength of 1454 MPa but fractured at a lower strain of 2.7%.
- (4). The combination of empirical parameters calculation and CALPHAD calculation to design HEAs with desired microstructures and properties were demonstrated to be an effective method based on the preliminary results in the present study.

A single-phase MoNbCrVTi alloy has been successfully designed and prepared based on the empirical parameters calculations and CALPHAD modeling. However, in the future, it is imperative that more efforts should be dedicated to further characterize the microstructure, enhance the alloy's ductility, and to investigate the irradiation resistance and corrosion behavior in simulated conditions under which the current cladding materials are being used. Therefore, the feasibility of HEAs used as cladding materials in the nuclear industry could be properly evaluated.

## Acknowledgments

The authors gratefully acknowledge the financial support from the Key Program of the Chinese Academy of Sciences (ZDRW-CN-2017-1).

## Appendix A. Supplementary data

Supplementary data to this article can be found online at <https://doi.org/10.1016/j.intermet.2018.11.001>.

## References

- [1] <https://www.iaea.org/PRIS/WorldStatistics/OperationalReactorsByType.aspx>.
- [2] I. Charit, Accident tolerant nuclear fuels and cladding materials, *J. Occup. Med.* 70 (2) (2018) 173–175, <https://doi.org/10.1007/s11837-017-2701-3>.
- [3] Z. Duan, H. Yang, Y. Satoh, K. Murakami, S. Kano, Z. Zhao, J. Shen, H. Abe, Current status of materials development of nuclear fuel cladding tubes for light water reactors, *Nucl. Eng. Des.* 316 (2017) 131–150 <https://doi.org/10.1016/j.nucengdes.2017.02.031>.
- [4] K.A. Terrani, S.J. Zinkle, L.L. Snead, Advanced oxidation-resistant iron-based alloys for LWR fuel cladding, *J. Nucl. Mater.* 448 (1–3) (2014) 420–435, <https://doi.org/10.1016/j.jnucmat.2013.06.041>.
- [5] S.J. Zinkle, K.A. Terrani, J.C. Gehin, L.J. Ott, L.L. Snead, Accident tolerant fuels for LWRs: a perspective, *J. Nucl. Mater.* 448 (1–3) (2014) 374–379, <https://doi.org/10.1016/j.jnucmat.2013.12.005>.
- [6] B.A. Pint, K.A. Terrani, Y. Yamamoto, L.L. Snead, Material selection for accident tolerant fuel cladding, *Mater. Mater. Trans. 2* (3) (2015) 190–196, <https://doi.org/10.1007/s40553-015-0056-7>.
- [7] R.B. Rebak, Versatile oxide films protect FeCrAl alloys under normal operation and accident conditions in light water power reactors, *J. Occup. Med.* 70 (2) (2018) 176–185, <https://doi.org/10.1007/s11837-017-2705-z>.
- [8] Y. Yamamoto, B.A. Pint, K.A. Terrani, K.G. Field, Y. Yang, L.L. Snead, Development and property evaluation of nuclear grade wrought FeCrAl fuel cladding for light water reactors, *J. Nucl. Mater.* 467 (2015) 703–716 <https://doi.org/10.1016/j.jnucmat.2015.10.019>.
- [9] S. Dryepondt, K.A. Unocic, D.T. Hoelzer, C.P. Massey, B.A. Pint, Development of low-Cr ODS FeCrAl alloys for accident-tolerant fuel cladding, *J. Nucl. Mater.* 501 (2018) 59–71 <https://doi.org/10.1016/j.jnucmat.2017.12.035>.
- [10] B. Cheng, P. Chou, Y.-J. Kim, Evaluations of Mo-alloy for light water reactor fuel cladding to enhance accident tolerance, *EPJ Nuclear Sci. Technol.* 2 (2016).
- [11] B.R. Maier, B.L. Garcia-Diaz, B. Hauch, L.C. Olson, R.L. Sindelar, K. Sridharan, Cold spray deposition of Ti2AlC coatings for improved nuclear fuel cladding, *J. Nucl. Mater.* 466 (2015) 712–717 <https://doi.org/10.1016/j.jnucmat.2015.06.028>.
- [12] K. Yueh, K.A. Terrani, Silicon carbide composite for light water reactor fuel assembly applications, *J. Nucl. Mater.* 448 (1) (2014) 380–388 <https://doi.org/10.1016/j.jnucmat.2013.12.004>.
- [13] J.-W. Yeh, S.K. Chen, S.J. Lin, J.Y. Gan, T.S. Chin, T.T. Shun, C.H. Tsau, S.Y. Chang, Nanostructured high-entropy alloys with multiple principal elements: novel alloy design concepts and outcomes, *Adv. Eng. Mater.* 6 (5) (2004) 299–303, <https://doi.org/10.1002/adem.200300567>.
- [14] J.-W. Yeh, Recent progress in high-entropy alloys, *Ann. Chim. Sci. Mat.* 31 (6) (2006) 633–648, <https://doi.org/10.3166/acsm.31.633-648>.
- [15] B. Cantor, I.T.H. Chang, P. Knight, A.J.B. Vincent, Microstructural development in equiatomic multicomponent alloys, *Mater. Sci. Eng., A* 375–377 (2004) 213–218, <https://doi.org/10.1016/j.msea.2003.10.257>.
- [16] O.N. Senkov, J.M. Scott, S.V. Senkova, D.B. Miracle, C.F. Woodward, Microstructure and room temperature properties of a high-entropy TaNbHfZrTi alloy, *J. Alloy. Comp.* 509 (20) (2011) 6043–6048, <https://doi.org/10.1016/j.jallcom.2011.02.171>.
- [17] B. Kang, J. Lee, H.J. Ryu, S.H. Hong, Ultra-high strength WNbMoTaV high-entropy alloys with fine grain structure fabricated by powder metallurgical process, *Mater. Sci. Eng., A* (2017), <https://doi.org/10.1016/j.msea.2017.12.021>.
- [18] X. Gao, Y. Lu, B. Zhang, N. Liang, G. Wu, G. Sha, J. Liu, Y. Zhao, Microstructural origins of high strength and high ductility in an AlCoCrFeNi2.1 eutectic high-entropy alloy, *Acta Mater.* 141 (2017) 59–66 <https://doi.org/10.1016/j.actamat.2017.07.041>.
- [19] T. Nagase, S. Anada, P.D. Rack, J.H. Noh, H. Yasuda, H. Mori, T. Egami, Electron-irradiation-induced structural change in Zr–Hf–Nb alloy, *Intermetallics* 26 (2012) 122–130, <https://doi.org/10.1016/j.intermet.2012.02.015>.
- [20] T. Nagase, S. Anada, P.D. Rack, J.H. Noh, H. Yasuda, H. Mori, T. Egami, MeV electron-irradiation-induced structural change in the bcc phase of Zr–Hf–Nb alloy with an approximately equiatomic ratio, *Intermetallics* 38 (2013) 70–79, <https://doi.org/10.1016/j.intermet.2013.02.009>.
- [21] S.-q. Xia, Z. Wang, T.-f. Yang, Y. Zhang, Irradiation behavior in high entropy alloys, *Journal of Iron and Steel Research International* 22 (10) (2015) 879–884.
- [22] N.D. Stepanov, N.Y. Yurchenko, V.S. Sokolovsky, M.A. Tikhonovsky, G.A. Salishchev, An AlNbTiVZr<sub>0.5</sub> high-entropy alloy combining high specific strength and good ductility, *Mater. Lett.* 161 (2015) 136–139 <https://doi.org/10.1016/j.matlet.2015.08.099>.
- [23] O.N. Senkov, G.B. Wilks, J.M. Scott, D.B. Miracle, Mechanical properties of Nb<sub>25</sub>Mo<sub>25</sub>Ta<sub>25</sub>W<sub>25</sub> and V<sub>20</sub>Nb<sub>20</sub>Mo<sub>20</sub>Ta<sub>20</sub>W<sub>20</sub> refractory high entropy alloys, *Intermetallics* 19 (5) (2011) 698–706, <https://doi.org/10.1016/j.intermet.2011.01.004>.
- [24] O.N. Senkov, S. Rao, K.J. Chaput, C. Woodward, Compositional effect on microstructure and properties of NbTiZr-based complex concentrated alloys, *Acta Mater.* (2018), <https://doi.org/10.1016/j.actamat.2018.03.065>.

- [25] Y. Qiu, S. Thomas, M.A. Gibson, H.L. Fraser, K. Pohl, N. Birbilis, Microstructure and corrosion properties of the low-density single-phase compositionally complex alloy AlTiVCr, *Corrosion Sci.* 133 (2018) 386–396 <https://doi.org/10.1016/j.corsci.2018.01.035>.
- [26] B. Gorr, F. Müller, M. Azim, H.-J. Christ, T. Müller, H. Chen, A. Kauffmann, M. Heilmair, High-temperature oxidation behavior of refractory high-entropy alloys: effect of alloy composition, *Oxid. Metals* (2017) 1–11, <https://doi.org/10.1007/s11085-016-9696-y>.
- [27] C. XIANG, W. Jiazheng, F. Huameng, H. En-Hou, H. ZHANG, W. Jianqiu, Z. ZHANG, Corrosion behavior of several high-entropy alloys in high temperature high pressure water, *J. Chin. Soc. Corrosion Protect* 36 (2) (2016) 107–112.
- [28] G.D. Sathiurai, P.P. Bhattacharjee, Effect of cold-rolling strain on the evolution of annealing texture of equiatomic CoCrFeMnNi high entropy alloy, *Mater. Char.* 109 (2015) 189–197, <https://doi.org/10.1016/j.matchar.2015.09.027>.
- [29] S.J. Sun, Y.Z. Tian, H.R. Lin, X.G. Dong, Y.H. Wang, Z.J. Zhang, Z.F. Zhang, Enhanced strength and ductility of bulk CoCrFeMnNi high entropy alloy having fully recrystallized ultrafine-grained structure, *Mater. Des.* 133 (2017) 122–127 <https://doi.org/10.1016/j.matdes.2017.07.054>.
- [30] C.J. Tong, Y.L. Chen, S.K. Chen, J.W. Yeh, T.T. Shun, C.H. Tsau, S.J. Lin, S.Y. Chang, Microstructure characterization of AlxCrxCuFeNi high-entropy alloy system with multiprincipal elements, *Metall. Mater. Trans.* 36A (4) (2005) 881–893, <https://doi.org/10.1007/s11661-005-0283-0>.
- [31] Y. Dong, K. Zhou, Y. Lu, X. Gao, T. Wang, T. Li, Effect of vanadium addition on the microstructure and properties of AlCoCrFeNi high entropy alloy, *Mater. Des.* 57 (2014) 67–72, <https://doi.org/10.1016/j.matdes.2013.12.048>.
- [32] T. Bhattacharjee, I.S. Wani, S. Sheikh, I.T. Clark, T. Okawa, S. Guo, P.P. Bhattacharjee, N. Tsuji, Simultaneous strength-ductility enhancement of a nano-lamellar AlCoCrFeNi<sub>2.1</sub> eutectic high entropy alloy by cryo-rolling and annealing, *Sci. Rep.* 8 (1) (2018) 3276, <https://doi.org/10.1038/s41598-018-21385-y>.
- [33] Y. Shi, L. Collins, R. Feng, C. Zhang, N. Balke, P.K. Liaw, B. Yang, Homogenization of AlxCrCrFeNi high-entropy alloys with improved corrosion resistance, *Corrosion Sci.* (2018), <https://doi.org/10.1016/j.corsci.2018.01.030>.
- [34] O.N. Senkov, J.M. Scott, S.V. Senkova, F. Meisenkothen, D.B. Miracle, C.F. Woodward, Microstructure and elevated temperature properties of a refractory TaNbHfZrTi alloy, *J. Mater. Sci.* 47 (9) (2012) 4062–4074, <https://doi.org/10.1007/s10853-012-6260-2>.
- [35] O.N. Senkov, S.L. Semiatin, Microstructure and properties of a refractory high-entropy alloy after cold working, *J. Alloy. Comp.* 649 (2015) 1110–1123 <https://doi.org/10.1016/j.jallcom.2015.07.209>.
- [36] F. Granberg, K. Nordlund, M.W. Ullah, K. Jin, C. Lu, H. Bei, L.M. Wang, F. Djurabekova, W.J. Weber, Y. Zhang, Mechanism of radiation damage reduction in equiatomic multicomponent single phase Alloys, *Phys. Rev. Lett.* 116 (13) (2016) 8, <https://doi.org/10.1103/PhysRevLett.116.135504>.
- [37] N.A.P.K. Kumar, C. Li, K.J. Leonard, H. Bei, S.J. Zinkle, Microstructural stability and mechanical behavior of FeNiMnCr high entropy alloy under ion irradiation, *Acta Mater.* 113 (2016) 230–244, <https://doi.org/10.1016/j.actamat.2016.05.007>.
- [38] J. Wang, X. Li, J. Wang, E.-h. Han, Development of a scratch electrode system in high temperature high pressure water, *Corrosion Sci.* 95 (2015) 125–132 <https://doi.org/10.1016/j.corsci.2015.03.006>.
- [39] W. Zhang, R. Tang, Z.B. Yang, C.H. Liu, H. Chang, J.J. Yang, J.L. Liao, Y.Y. Yang, N. Liu, Preparation, structure, and properties of an AlCrMoNbZr high-entropy alloy coating for accident-tolerant fuel cladding, *Surf. Coatings. Technol.* 347 (2018) 13–19 <https://doi.org/10.1016/j.surfcoat.2018.04.037>.
- [40] A. Takeuchi, A. Inoue, Classification of bulk metallic glasses by atomic size difference, heat of mixing and period of constituent elements and its application to characterization of the main alloying element, *Mater. Trans.* 46 (12) (2005) 2817–2829.
- [41] X. Yang, Y. Zhang, Prediction of high-entropy stabilized solid-solution in multi-component alloys, *Mater. Chem. Phys.* 132 (2–3) (2012) 233–238, <https://doi.org/10.1016/j.matchemphys.2011.11.021>.
- [42] Y. Zhang, X. Yang, P. Liaw, Alloy design and properties optimization of high-entropy alloys, *J. Occup. Med.* 64 (7) (2012) 830–838, <https://doi.org/10.1007/s11837-012-0366-5>.
- [43] Y.D. Wu, Y.H. Cai, X.H. Chen, T. Wang, J.J. Si, L. Wang, Y.D. Wang, X.D. Hui, Phase composition and solid solution strengthening effect in TiZrNbMoV high-entropy alloys, *Mater. Des.* 83 (2015) 651–660, <https://doi.org/10.1016/j.matdes.2015.06.072>.
- [44] <https://www.webelements.com>.
- [45] [http://crysdb.nims.go.jp/index\\_en.html](http://crysdb.nims.go.jp/index_en.html).
- [46] O.N. Senkov, G.B. Wilks, D.B. Miracle, C.P. Chuang, P.K. Liaw, Refractory high-entropy alloys, *Intermetallics* 18 (9) (2010) 1758–1765, <https://doi.org/10.1016/j.intermet.2010.05.014>.
- [47] O.N. Senkov, C.F. Woodward, Microstructure and properties of a refractory NbCrMo<sub>0.5</sub>Ta<sub>0.5</sub>TiZr alloy, *Mater. Sci. Eng., A* 529 (2011) 311–320, <https://doi.org/10.1016/j.msea.2011.09.033>.
- [48] O.N. Senkov, D.B. Miracle, Effect of the atomic size distribution on glass forming ability of amorphous metallic alloys, *Mater. Res. Bull.* 36 (12) (2001) 2183–2198 [https://doi.org/10.1016/S0025-5408\(01\)000715-2](https://doi.org/10.1016/S0025-5408(01)000715-2).
- [49] O.N. Senkov, S.V. Senkova, C. Woodward, D.B. Miracle, Low-density, refractory multi-principal element alloys of the Cr–Nb–Ti–V–Zr system: microstructure and phase analysis, *Acta Mater.* 61 (5) (2013) 1545–1557 <https://doi.org/10.1016/j.actamat.2012.11.032>.
- [50] O.N. Senkov, F. Zhang, J.D. Miller, Phase composition of a CrMo<sub>0.5</sub>NbTa<sub>0.5</sub>TiZr high entropy alloy: comparison of experimental and simulated data, *Entropy* 15 (9) (2013) 3796–3809, <https://doi.org/10.3390/e15093796>.
- [51] H.W. Yao, J.W. Qiao, J.A. Hawk, H.F. Zhou, M.W. Chen, M.C. Gao, Mechanical properties of refractory high-entropy alloys: experiments and modeling, *J. Alloy. Comp.* 696 (2017) 1139–1150 <https://doi.org/10.1016/j.jallcom.2016.11.188>.
- [52] B. Zhang, Y. Mu, M.C. Gao, W.J. Meng, S.M. Guo, On single-phase status and segregation of an as-solidified septenary refractory high entropy alloy, *MRS Communications* (2017) 1–6, <https://doi.org/10.1557/mrc.2017.7>.
- [53] H.W. Yao, J.W. Qiao, M.C. Gao, J.A. Hawk, S.G. Ma, H.F. Zhou, Y. Zhang, NbTaV–(Ti,W) refractory high-entropy alloys: experiments and modeling, *Mater. Sci. Eng., A* 674 (2016) 203–211, <https://doi.org/10.1016/j.msea.2016.07.102>.
- [54] B. Zhang, M.C. Gao, Y. Zhang, S.M. Guo, Senary refractory high-entropy alloy CrxMonNbTaVW, *Calphad* 51 (2015) 193–201 <https://doi.org/10.1016/j.calphad.2015.09.007>.
- [55] M.C. Gao, B. Zhang, S. Yang, S.M. Guo, Senary refractory high-entropy alloy HfNbTaTiIVZr, *Metallurgical and Materials Transactions a-Physical Metallurgy and Materials Science* 47A (7) (2016) 3333–3345, <https://doi.org/10.1007/s11661-015-3105-z>.
- [56] Tazuddin, N.P. Gurao, K. Biswas, In the quest of single phase multi-component multiprincipal high entropy alloys, *J. Alloy. Comp.* 697 (2017) 434–442, <https://doi.org/10.1016/j.jallcom.2016.11.383>.
- [57] B. Gludovatz, A. Hohenwarter, D. Catoor, E.H. Chang, E.P. George, R.O. Ritchie, A fracture-resistant high-entropy alloy for cryogenic applications, *Science* 345 (6201) (2014) 1153–1158, <https://doi.org/10.1126/science.1254581>.
- [58] F. Otto, Y. Yang, H. Bei, E.P. George, Relative effects of enthalpy and entropy on the phase stability of equiatomic high-entropy alloys, *Acta Mater.* 61 (7) (2013) 2628–2638, <https://doi.org/10.1016/j.actamat.2013.01.042>.
- [59] E. Scheil, Comments on the layer crystal formation, *Z. Metallkd* 34 (1942) 70–72.
- [60] G.H. Gulliver, The quantitative effect of rapid cooling upon the constitution of binary alloys, *J. Inst. Met.* 9 (1) (1913) 120–157.
- [61] M.C. Gao, Design of high-entropy alloys, in: M.C. Gao, J.-W. Yeh, P.K. Liaw, Y. Zhang (Eds.), *High-entropy Alloys: Fundamentals and Applications*, Springer, Cham, Switzerland, 2016, pp. 369–398.
- [62] L. Vegard, Die Konstitution der Mischkristalle und die Raumfüllung der Atome, *Zeitschrift für Physik A Hadrons und Nukleii* 5 (1) (1921) 17–26.
- [63] B. Ren, Z.X. Liu, D.M. Li, L. Shi, B. Cai, M.X. Wang, Effect of elemental interaction on microstructure of CuCrFeNiMn high entropy alloy system, *J. Alloy. Comp.* 493 (1–2) (2010) 148–153, <https://doi.org/10.1016/j.jallcom.2009.12.183>.
- [64] C.-M. Lin, C.-C. Juan, C.-H. Chang, C.-W. Tsai, J.-W. Yeh, Effect of Al addition on mechanical properties and microstructure of refractory AlxHfNbTaTiZr alloys, *J. Alloy. Comp.* 624 (2015) 100–107, <https://doi.org/10.1016/j.jallcom.2014.11.064>.
- [65] C.-C. Juan, K.-K. Tseng, W.-L. Hsu, M.-H. Tsai, C.-W. Tsai, C.-M. Lin, S.-K. Chen, S.-J. Lin, J.-W. Yeh, Solution strengthening of ductile refractory HfMoxNbTaTiZr high-entropy alloys, *Mater. Lett.* 175 (2016) 284–287, <https://doi.org/10.1016/j.matlet.2016.03.133>.
- [66] U.S. Hsu, U.D. Hung, J.W. Yeh, S.K. Chen, Y.S. Huang, C.C. Yang, Alloying behavior of iron, gold and silver in AlCoCrCuNi-based equimolar high-entropy alloys, *Mater. Sci. Eng., A* 460 (2007) 403–408 <https://doi.org/10.1016/j.msea.2007.01.122>.
- [67] J. Pi, Y. Pan, H. Zhang, L. Zhang, Microstructure and properties of AlCrFeCuNi<sub>x</sub> (0.6 ≤ x ≤ 1.4) high-entropy alloys, *Mater. Sci. Eng., A* 534 (2012) 228–233, <https://doi.org/10.1016/j.msea.2011.11.063>.
- [68] B.S. Murty, J.W. Yeh, S. Ranganathan, *High-entropy Alloys*, Butterworth-Heinemann, London, UK, 2014.
- [69] S. Maiti, W. Steurer, Structural-disorder and its effect on mechanical properties in single-phase TaNbHfZr high-entropy alloy, *Acta Mater.* 106 (2016) 87–97, <https://doi.org/10.1016/j.actamat.2016.01.018>.
- [70] X.D. Xu, P. Liu, S. Guo, A. Hirata, T. Fujita, T.G. Nieh, C.T. Liu, M.W. Chen, Nanoscale phase separation in a fcc-based CoCrCuFeNiAl<sub>0.5</sub> high-entropy alloy, *Acta Mater.* 84 (2015) 145–152, <https://doi.org/10.1016/j.actamat.2014.10.033>.
- [71] Y. Zhang, Y.J. Zhou, J.P. Lin, G.L. Chen, P.K. Liaw, Solid-solution phase formation rules for multi-component alloys, *Adv. Eng. Mater.* 10 (6) (2008) 534–538, <https://doi.org/10.1002/adem.200700240>.
- [72] S. Guo, C. Ng, J. Lu, C.T. Liu, Effect of valence electron concentration on stability of fcc or bcc phase in high entropy alloys, *J. Appl. Phys.* 109 (10) (2011) 103505, <https://doi.org/10.1063/1.3587228>.